Facile synthesis of ZnO nanorod arrays and hierarchical nanostructures for photocatalysis and gas sensor applications

Shuaishuai Ma[a], Rong Li[a], Changpeng Lv[a], Wei Xu[b], Xinglong Gou[a,*]

[a] Chemical Synthesis and Pollution Control Key Laboratory of Sichuan Province, College of Chemistry and Chemical Engineering, China West Normal University, 1# Shida Road, Nanchong 637000, People's Republic of China
[b] Ningbo Institute of Material Technology & Engineering, Chinese Academy of Sciences, Ningbo 315201, People's Republic of China

ARTICLE INFO

ABSTRACT

A facile one-step hydrothermal route was demonstrated to grow ZnO nanorod arrays and hierarchical nanostructures on arbitrary substrates without any catalysts and seeds coated before the reaction, which are prerequisite in the current two-step protocol. Meanwhile, ZnO nanoflowers composed of nanorods were obtained at the bottom of the autoclaves in the absence of substrates. An in situ spontaneous-seeds-assisted growth mechanism was tentatively proposed on the basis of the experimental data to explain the growth process of ZnO nanostructures. Moreover, the obtained ZnO nanorod arrays exhibited superior photocatalytic activity for decomposing methyl orange, and the nanoflowers showed better gas sensing performance towards some flammable gases and corrosive vapors with high sensitivity, rapid response–recovery characteristics, good selectivity and long-term stability.

© 2011 Elsevier B.V. All rights reserved.

1. Introduction

One-dimensional (1D) nanostructures (rods, wires, tubes and belts) have been attracting a great deal of research interest for decades due to their unique properties and potential to revolutionize broad areas of nanotechnology [1–3]. However, the assembly and integration of 1D nanomaterials into three-dimensional arrays or hierarchical structures are desirable for many applications, including microelectronic devices, chemical and biological sensing, energy conversion and storage, light-emitting displays, and catalysis [4–7]. Various physic and chemical routes have been developed to fabricate nanoarrays and hierarchical nanostructures on demanded substrates [8–11] for facile addressing, transport, contact, and detection, yet the direct fabrication of them on arbitrary substrates via simple and cost-effective techniques remains a significant challenge.

Zinc oxide (ZnO) is a key technological material with fantastic properties and potential applications in numerous fields. Recently, highly ordered ZnO nanoarrays and hierarchical nanostructures composed of 1D building blocks exhibited promising perspective for application in multifunctional nanodevices and nanosystems such as ultraviolet nanolasers [12], gas sensors and biosensors [13,14], nano-optoelectronics [15], piezoelectric nano-

generators [16], solar cells [17], field emitters and flat panel displays [18], light emitting diodes [19], and excellent photocatalysts [20]. As a response, considerable efforts have been made to grow high quality ZnO nanoarrays on demanded substrates with ideal geometry, array density, and length–diameter-ratio for optimizing their potential applications. Currently, ZnO nanoarrays can be prepared by template-assisted growth [7,11], photolithography [21], electrodeposition [22], chemical vapour deposition (CVD) and thermal evaporation [23], oxidation of Zn foils in both gas-phase and solution-phase [10], and hydrothermal routes [13]. Among these synthetic methods, solution-phase technique is proved to be relatively simple and cost-effective. However, the current solution-phase approaches for growth oriented ZnO nanoarrays on demanded substrates usually need complex multi-step process and coating the substrates with expensive catalysts or ZnO seed layers before reaction [9,24,25]. Therefore, inexpensive and catalyst/seed-free technique is essential for growth of ZnO nanoarrays and hierarchical nanostructures with high quality on any substrates [26–28].

Here, we demonstrate that orderly aligned ZnO nanorods can be grown on various substrates (conductive copper foils, rigid polytetrafluoroethylene plates, nonconductive and flexible plastics) via a facile one-step hydrothermal route in the presence of D-fructose. This protocol does not need pre-deposition of any catalysts and seeds before reaction, and thus is simple and cost-effective. Meanwhile, ZnO nanoflowers composed of nanorods were obtained in the absence of substrates. The crystallographic phase, morphol-

* Corresponding author.
   E-mail address: gouxlr@126.com (X. Gou).

ogy, microstructures, photocatalytic and sensing performance of the products were characterized by a series of techniques. The results show that both of the nanorod arrays and nanoflowers can be used as superior photocatalysts with high activity for decomposing organic dyes, and exhibit excellent gas sensing performance. However, performance difference between the obtained nanorod arrays and the nanoflowers was also observed due to their different microstructures and orientation of the nanorods.

2. Experimental

2.1. Preparation of ZnO nanorod arrays and hierarchical nanostructures

All reagents were of analytical grade and were used as purchased without further purification. ZnO nanorod arrays were grown on various substrates including conductive Cu foil and nonconductive plastic plates via a simple hydrothermal route without using any catalysts or ZnO seeds. In a typical synthesis, 5 mL of NaOH ($3 \, mol \, L^{-1}$) was added into an equal volume of $Zn(NO_3)_2$ aqueous solution ($0.5 \, mol \, L^{-1}$) with continuous stirring, yielding a white suspension. After stirring for 5 min, 0.1 g D-fructose was added and the mixture was stirred at room temperature for another 30 min, resulting in the formation of a buff suspension. Subsequently, the suspension was transferred into a Teflon-lined autoclave with a capacity of 25 mL. Then, a piece of 2 cm × 2.5 cm Cu foil used as the substrate for the growth of ZnO nanorod arrays was inserted into the autoclave after being ultrasonically cleaned in succession with acetone, ethanol, isopropyl alcohol and de-ionized water. Finally, the autoclave was sealed and kept at 180 °C for 12 h. Upon cooling to room temperature, the Cu foil was firmly covered with a dense film of white deposit. After being rinsed with distilled water for several times, The Cu foil covered with the products was dried in air for further characterizations. Meanwhile, ZnO nanoflowers were obtained at the bottom of the autoclave in the absence of the substrates. To further investigate the generality of this catalyst and seed-free growth method for ZnO nanoarrays on arbitrary substrates, nonconductive substrates including rigid polytetrafluoroethylene (PTFE) plates and flexible plastic sheets were also used keeping the other procedures unchanged.

2.2. Sample characterizations

The phase purity, crystal structure and morphologies of the products were characterized using a combination of the following techniques: X-ray diffraction (XRD, Rigaku Ultima IV, Cu Kα radiation), scanning electron microscope (SEM, JEOL JSM-6510LV) coupled with an energy-dispersive X-ray spectroscopy (EDS, Oxford instruments X-Max), transmission electron microscope (TEM, FEI Tecnai F20), high resolution TEM (HRTEM), selected area electron diffraction (SAED), Brunauer–Emmett–Teller (BET) nitrogen adsorption–desorption (Quanta Chrome Nova 1000 Gas Sorption Analyzer), and Fourier transform infrared spectroscopy (FTIR, Thermo Scientific Nicolet 6700 FT-IR Spectrometer).

2.3. Evaluation of photocatalytic activity

Photocatalytic activities of the ZnO products were evaluated by decomposition of methyl orange (MO) as a model system. First, 50 mg of the as-prepared ZnO samples (the ZnO nanorods were peeled off from the Cu substrate by ultrasonic treatment in a general ultrasonic cleaner, and were used in the form of powder for the photocatalysis, BET, and gas sensors measurements) were added into 200 mL of MO aqueous solution with an initial concentration of $10 \, mg \, L^{-1}$ in a cylindrical glass jacketed reactor equipped with
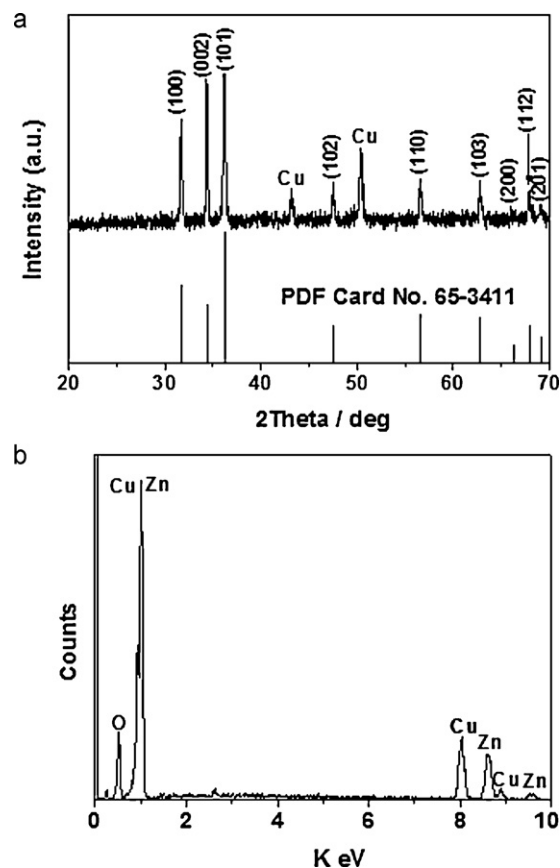

Fig. 1. XRD pattern (a) and EDS spectrum (b) of the white precipitates on the Cu substrate produced through hydrothermal reaction, indicating the products are high-purity ZnO. The signals of Cu in both the XRD pattern and the EDS spectrum were originated from the copper substrate.

reflux water to keep the reaction temperature constant. Subsequently, the suspension of ZnO and MO was magnetically stirred in dark for 30 min before irradiating with a 250 W high-pressure mercury lamp (GY-250, λ = 365 nm), which was 35 cm above the surface of the suspension containing ZnO powder and MO. During the process of photodegradation, 5 mL of the suspension was sampled every 5 min. After centrifugation, the supernatant was kept for UV–vis characterization to determine the contents of MO.

2.4. Measurement of gas sensing performance

Gas sensing performances of the ZnO products were tested using a computer controlled WS-60A gas sensor measurement system (Zhengzhou Winsen Electronics Technology Co., Ltd, China). The configuration, fabrication procedure and sensing performance measurement of the ZnO sensors were similar to our previous report [29]. Sensitivity (S) of the sensor is defined as $S = R_{air}/R_{gas}$, where R_{air} and R_{gas} are the stationary electrical resistance of the sensor in air and in the test gas, respectively.

3. Results and discussion

3.1. Structure and morphology of the products

Phase purity and crystallographic structure of the white deposits on the Cu substrate after hydrothermal reaction were determined by XRD analysis, as shown in Fig. 1(a). Except for the two diffraction peaks from the Cu substrate at 2 theta degree of 43.2° and 50.4°, all the peaks can be readily indexed to hexagonal wurtzite
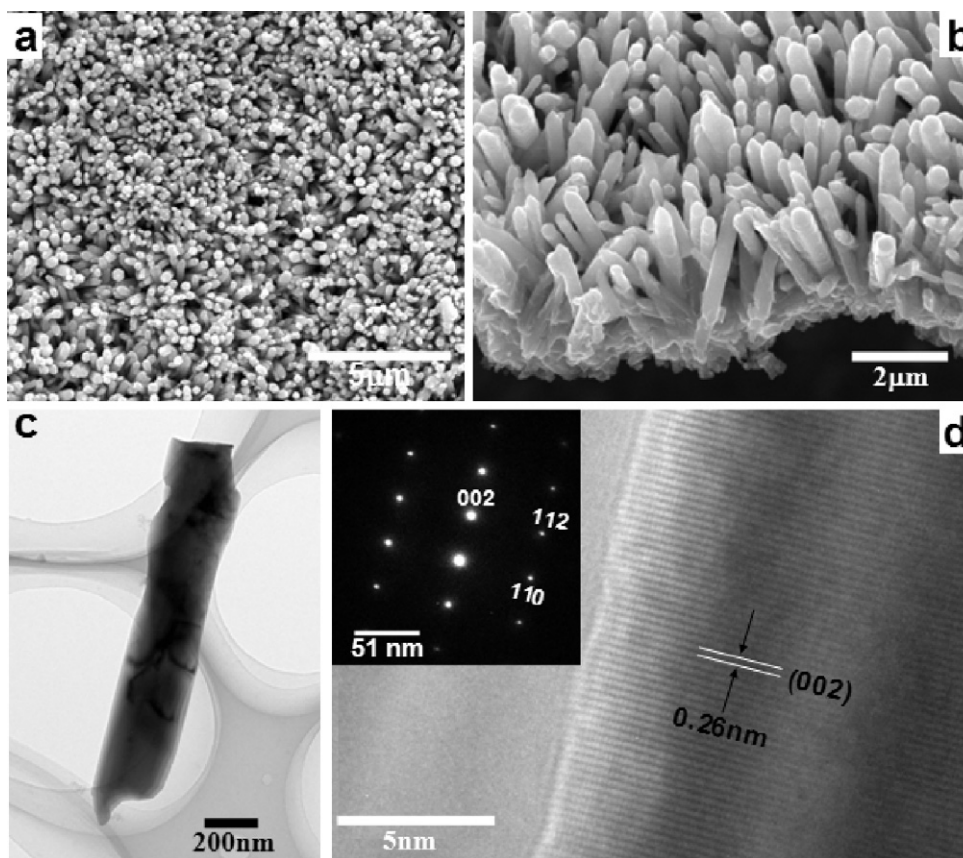
Fig. 2. (a and b) SEM images of the ZnO nanorod arrays grown on the Cu substrate with high density. (c and d) TEM and HRTEM images of an individual ZnO nanorod peeled off from the substrate during the preparation of TEM sample. Inset of (d) is the corresponding SAED pattern, indicating the ZnO nanorods grew along [0 0 2] direction.

structured ZnO with lattice parameters, a = 3.249 Å, c = 5.206 Å, in good agreement with the standard data (JCPDS Card No. 65-3411). In addition, the peak intensity of (0 0 2) plane of the ZnO film is relatively stronger than that of the standard data, indicating that the ZnO products have a preferred orientation along the (0 0 2) plane. EDS analysis (Fig. 1b) further confirms that the white deposits on the Cu substrate are only composed of Zn and O with an atomic ratio of about 1:1, in accordance with the stoichiometry of ZnO.
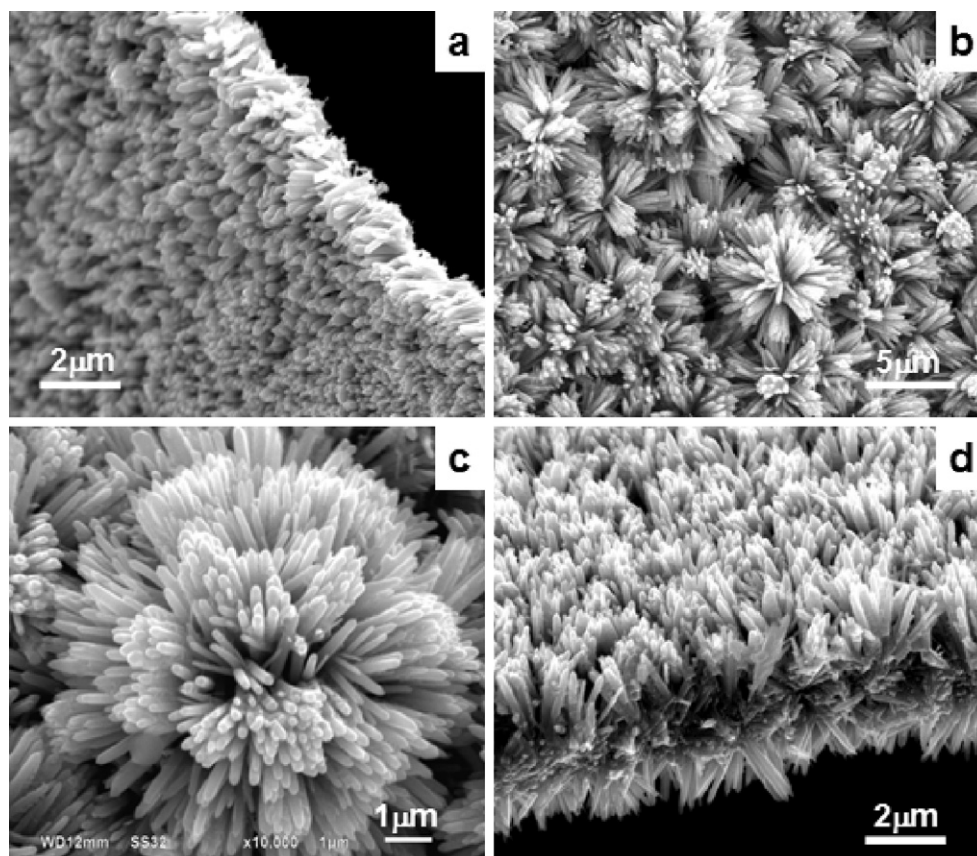
The morphology and microstructure of the ZnO products deposited on the Cu substrate were characterized by SEM and TEM. Fig. 2(a) and (b) shows the typical SEM images with different magnifications. The top-view image at low magnification in Fig. 2(a) reveals that the copper substrate is uniformly covered with a dense film of ZnO nanorods, which grow vertically to the substrate with an almost uniform height of about 2.5 μm. The cross-section view image with higher magnification in Fig. 2(b) indicates that the diameters of the ZnO nanorods are in the range of 170–260 nm. Note that we did not use any catalysts and pre-deposited ZnO seed layers before reaction, which are usually employed for the growth of ZnO nanoarrays on the substrate [9]. However, we did observe from the cross-section view a thin layer of ZnO nanocrystals at the root of the nanorod arrays, which might be deposited on the substrate prior to the growth of the nanoarrays. We believe this in situ spontaneous seed crystals are responsible for the growth of the ZnO nanorod arrays, which will be discussed in the later part.

The nanorod morphology of the ZnO nanoarrays was further verified by TEM observation. Fig. 2(c) displays a typical TEM image of an individual ZnO nanorod peeled off from the copper substrate by ultrasonic treatment. The corresponding HRTEM image in Fig. 2(d) shows clear lattice planes perpendicular to the growth direction of

the ZnO nanorod. The lattice spacing was determined to be 0.26 nm, corresponding to the interspacing of the (0 0 2) plane of wurtzite structured ZnO. The SAED pattern in the inset of Fig. 2(d) affirms the single crystallinity with the c-axis preferred orientation of the obtained ZnO nanorods. So, both the results of HRTEM and SAED analysis confirm that the ZnO nanorods are grown preferentially along the (0 0 2) direction, consistent with the XRD result in Fig. 1.

Other nonconductive substrates such as rigid PTFE plate and flexible plastic sheet were also investigated for growth of ZnO under the same conditions employed by the synthesis of ZnO nanorod arrays on copper foil. As expected, white deposits were produced in both cases. The white film tightly adhered to the PTFE plates as did on the Cu substrate, while the film on the flexible plastic sheet was relatively loose and was easy to be peeled off, making it possible to be transferred to other substrates for specific applications [15]. In addition, their microstructures are slightly different although both of them look like nanorod-arrays on the whole. Fig. 3(a) shows the cross-section view image of the ZnO film deposited on the rigid PTFE substrate, indicating that it consists of nanorods oriented nearly parallel to each other. This morphology and microstructure are more like the ZnO nanorod arrays grown on the copper foil. In contrast, the film deposited on the flexible plastic sheet is mainly composed of flower-like hierarchical nanostructures, which distributed densely and almost uniformly over the surface of the plastic substrate as shown in Fig. 3(b). The magnified view in Fig. 3(c) further manifests that each hierarchically nanostructured flower is actually made of numerous nanorods with a diameter ranging from 140 to 250 nm and a length of up to 3 μm. It was interesting that we also observed some dual-sided nanorod arrays, between which a thin layer of ZnO nanocrystals were sandwiched as shown in Fig. 3(d). The two types of ZnO nanoarrays were

Fig. 3. SEM images of the ZnO nanorod arrays grown on the nonconductive substrates such as rigid PTFE plates (a) and flexible plastic sheets (b–d), showing the subtle difference in the morphology and microstructure of the products grown on different substrates and different regions on the same substrate.

often found to be grown on different regions of the plastic surface, where convex and concave were observed due to the deformation of the flexible plastic sheet at high temperature and autogenous pressure. This growth mechanism will be discussed later.

On the other hand, the precipitates collected from the bottom of the autoclave in the presence or absence of substrates always exhibit the morphology of flower-like hierarchical nanostructures (hereinafter referred to as nanoflowers). Fig. 4(a) and (b) displays the typical SEM images at different resolutions of the product. Most of the nanoflowers could withstand ultrasonic treatment for the preparation of TEM sample and preserve its integrity in the TEM observation as shown in Fig. 4(c). Obviously, the nanoflowers were also composed of nanorods with an average diameter of about 180 nm, which linked together through their root segments. The region marked with a rectangle in one nanorod arm of the nanoflower was further magnified and shown in Fig. 4(d). Regular lattice fringes perpendicular to the growth direction of ZnO nanorods indicate that the grown nanorods are single crystalline. Moreover, the lattice spacing is about 0.52 nm, corresponding to the (0 0 1) planes of the wurtzite hexagonal ZnO. The corresponding SAED pattern in the inset further confirms the single crystallinity of the ZnO nanorods with the c-axis preferred orientation.

3.2. Growth mechanism of the ZnO nanoarrays and hierarchical nanostructures

Considering that there were no additional catalysts and ZnO seeds involved before the growth of ZnO nanoarrays, it is reasonable to presume that the formation of ZnO nanostructures in our case followed different mechanisms compared with the widely employed catalyst/seed-assisted two-step growth method [9]. On the basis of the above experiments, an in situ spontaneous-seeds-assisted growth mechanism is tentatively proposed and is schematically illustrated in Fig. 5. ZnO colloidal nuclei were first formed during the reaction. In the presence of rigid substrates such as copper and PTFE plate, the in situ spontaneous ZnO colloidal nuclei adsorbed tightly to the flat surface of the substrates and acted as crystal seeds to direct the growth of ZnO nanorod arrays as shown in the first route of Fig. 5. Therefore, we can observe a thin layer of ZnO nanocrystals at the root of the nanorod arrays in Fig. 1(b). When flexible plastic sheet was used as substrate, it could be soften and deformed at high temperature and autogenous pressure. The convex surface would raised the deposited ZnO seed layers with certain curvature, leading to the growth of flowerlike hierarchical nanostructures as shown in the second route of Fig. 5, whereas the concave part would leave some spaces between the seed layers and the concave surface of the substrate for the dual-sided growth of ZnO nanorods, which was supported by SEM observation in Fig. 2(b)–(d). It was because of the deformation of the plastic surface that the deposited ZnO nanocrystals could not tightly cling to the substrate, resulting in the grown ZnO film easy to be peeled off. Otherwise, the un-adsorbed ZnO colloidal nuclei in the presence or absence of substrates would grow by oriented attachment and re-crystallization to form nanoflowers as shown in the third route of Fig. 5, in accordance with the result of electronic microscopic observation in Fig. 4.

The role of D-fructose played was also investigated in the synthesis of ZnO nanostructures. The results showed that ZnO nanoflowers were always obtained at the bottom of the autoclave whether D-fructose was added or not, and the amount of D-fructose did not affect the morphology and microstructure of the products. However, we could not obtain ZnO film on any substrates without addition of D-fructose.
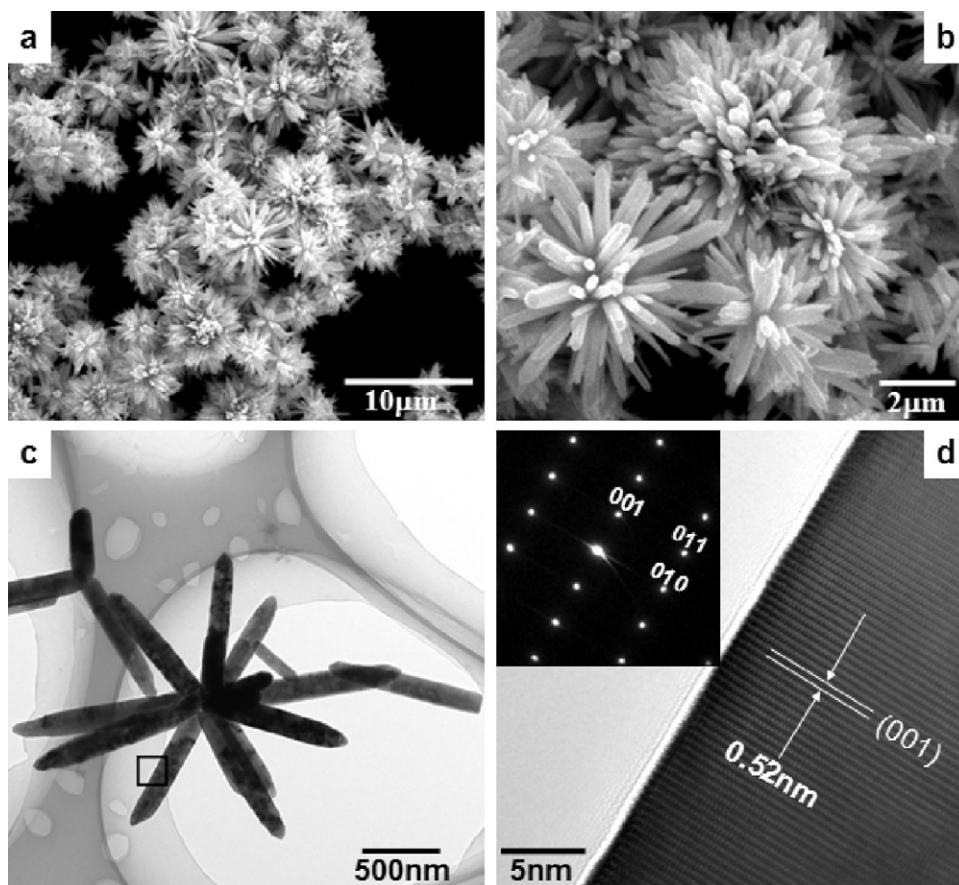
Fig. 4. (a and b) SEM images of the ZnO precipitates collected at the bottom of the autoclave. (c) TEM image of the flowerlike nanostructures composed of nanorods. (d) HRTEM image of the edge in one arm marked with a rectangle in panel (c). The inset is the SAED pattern of the selected nanorod.

XRD and EDS analyses further revealed that Cu foil were prone to be oxidized in the absence of D-fructose, as shown in Fig. 6. It was because of the oxidization of Cu foil that the copper oxides rather than ZnO film were grown on the Cu substrate. Once D-fructose was introduced into the reaction system, no copper oxides were formed on the Cu foil immersed in the solution whether Zn^{2+} was added

Fig. 5. Schematic illustration of the growth mechanism of the ZnO nanostructures in the presence or absence of substrates.

or not, suggesting that the oxidization of Cu foil could be completely suppressed by D-fructose. When both D-fructose and Zn^{2+} were added, ZnO film were grown on the Cu substrate as shown in Figs. 1 and 2. In this case, even if the ZnO nanoarrays were peeled off from the Cu substrate for XRD and EDS characterizations, no copper oxides were detected in the separated Cu substrate and ZnO nanoarrays, indicating that D-fructose acted as a reducing agent to prevent the Cu substrate from oxidization, and hence provide a restful substrate for landing of the in situ produced ZnO crystal seeds and further growth of ZnO nanoarrays on the Cu foil.

With increase of D-fructose, the adhesion of the ZnO film onto the substrate was enhanced, but the morphology of the ZnO film did not change with the amount of D-fructose. Therefore, D-fructose might also act as an adhesive in our experiments to link the in situ spontaneous ZnO colloidal nuclei onto the substrate as seed layers for the growth of ZnO film rather than as a molecule template proposed for the growth of ultrathin $ZnSnO_3$ nanowires [30]. During the reaction D-fructose molecules could adsorb on the surface of ZnO colloidal nuclei through coordination or electrostatic interactions. With the reaction temperature increasing dehydration and polymerization reactions occurred between D-fructose molecules, endowing the ZnO colloidal nuclei amphiphilic characters due to the in situ produced polysaccharide molecules or colloidal carbon [31], which was in favor of enhancing adhesion of the spontaneous ZnO nanocrystals to the substrates as seed coats for the growth of nanoarrays. After reaction the color of the solution became light brown, indicative of the dehydration and polymerization of D-fructose molecules. However, the FTIR spectra of the supernatant of the reaction system before/after reaction (Fig. 7A) and the ZnO
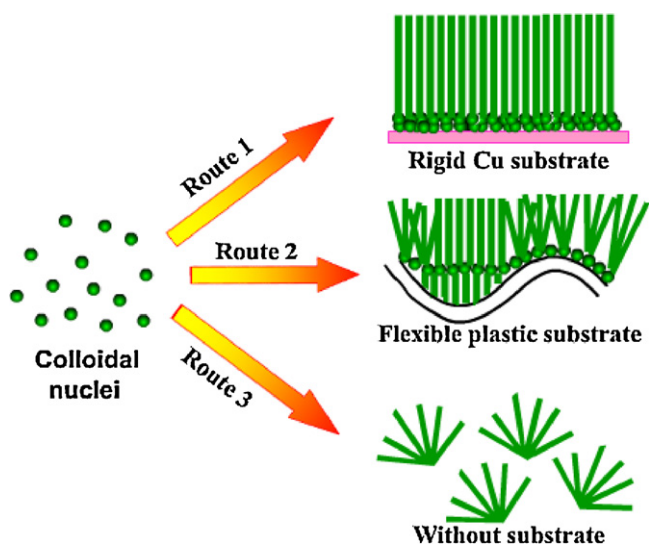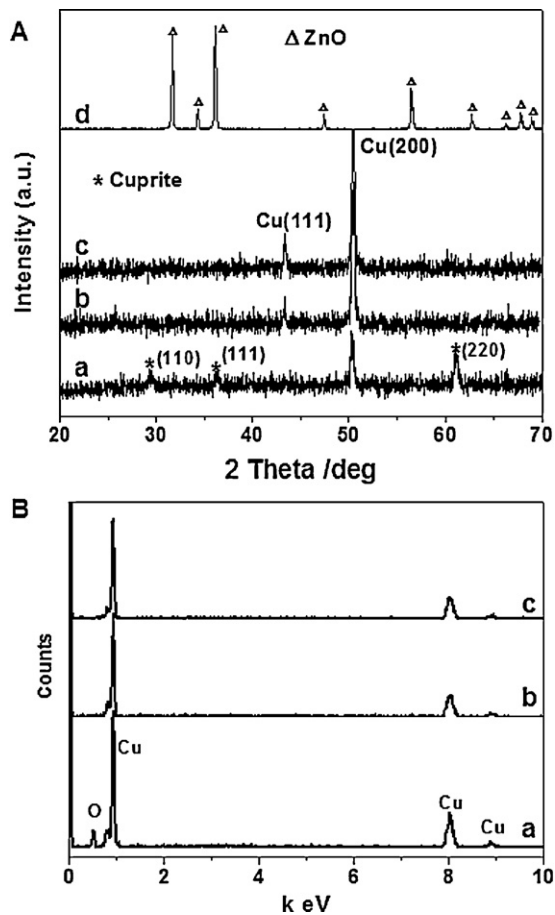
Fig. 6. XRD patterns (A) and EDS spectra (B) of the Cu substrate after reaction in the absence of D-fructose (a), the Cu substrate in the presence of D-fructose but without addition of Zn^{2+} (b), the Cu substrate after the deposited ZnO film was peeled off (c), and the separated ZnO powders (d). These data suggested that D-fructose in the reaction system acted as a reducing agent to prevent the Cu substrate from oxidization.

products prepared with/without addition of D-fructose (Fig. 7B) indicated that carbonization of D-fructose molecules was not serious, and the quantity of carbon doped in the ZnO products was too small to be detected by XRD and EDS analyses as shown in Fig. 6. A series of temperature-dependent experiments were also performed to investigate the polymerization of D-fructose and its effect on the quality of the ZnO film. When the reactions were carried out at the temperature range of 150–170 °C, we only obtained tenuous fractal ZnO films on the substrates. While the reaction temperatures were below 140 °C, there were nothing deposited on the substrates, because dehydration and polymerization of D-fructose molecules were insufficient below this temperature [31]. Thus it can be seen that higher temperature can promote the polymerization of D-fructose, resulting in enhancement of adhesion strength of ZnO nuclei to the substrate, and then improve the quality of the ZnO film deposited on the substrates.

Compared with the current multi-step process for preparation of ZnO nanoarrays, this catalysts and seeds-free one-step hydrothermal synthesis is relatively simple and cost-effective. Moreover, ZnO nanoarrays can be grown on arbitrary substrates including conductive/nonconductive and rigid/flexible ones at low temperature via this route, which is compatible with the semiconductor process technology and is suitable for fabrication of nanodevices [15]. The prepared ZnO nanoarrays on conductive or nonconductive substrates are expected to find wide applications in nanoelectronic, optical, electrochemical, solar cells, and
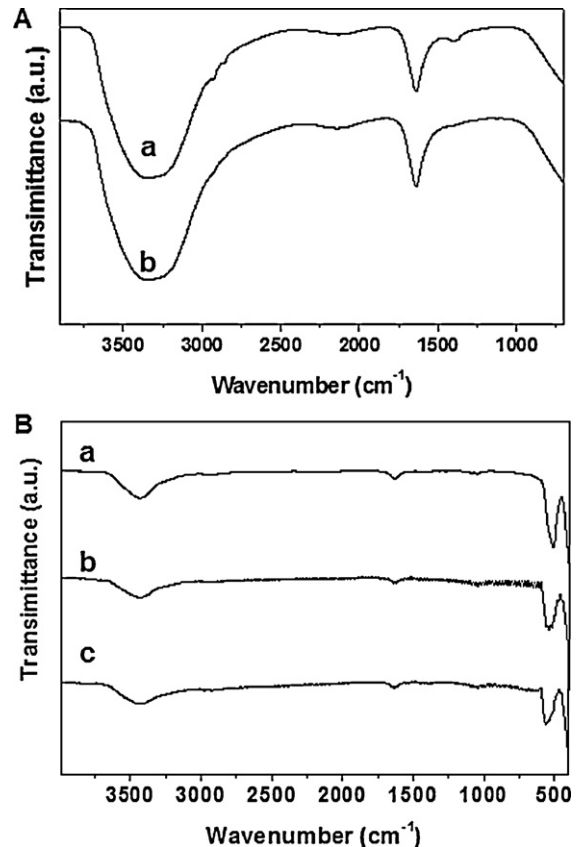
Fig. 7. (A) FTIR spectra of the supernatant of the reaction system before (a) and after reaction (b); (B) FTIR spectra of the ZnO powders prepared without addition of D-fructose (a), ZnO nanoflowers (b) and nanorod arrays (c) synthesized with the help of D-fructose.

photoelectrochemical fields. Herein, we investigated the photodegradation of organic dyes and gas sensing performance of the ZnO nanorods as well as nanoflowers to demonstrate their potential applications in environmental remediation and monitoring.

3.3. Photocatalytic activities of the ZnO samples

Before UV irradiation the reaction mixtures with different ZnO samples were continuously stirred for 30 min to reach absorption equilibrium. At this point, the absorbance values of the mixtures decreased by 0.67%, 0.80% and 0.40%, due to absorption of methyl orange (MO) molecules by the ZnO nanorods peeled off from the Cu substrate, ZnO nanoflowers collected from the bottom of the autoclave, and the commercial ZnO powders, respectively. This order is in good accordance with their specific surface areas: 20.2, 24.5, and 3.7 $m^2 g^{-1}$. Upon UV irradiation, the color of the MO solution with addition of ZnO nanorods was rapidly degraded with time, and the corresponding digital photographs were recorded and shown in Fig. 8(a). It can be seen that the MO solution was totally colorless after irradiation for 60 min, indicating the MO molecules had been completely photo-decomposed by ZnO nanorods. The results were further confirmed by the temporal UV–vis adsorption spectra in Fig. 8(b). The absorbance value decreased swiftly at the characteristic peak location (462 nm) of MO, and was very close to zero after 60 min irradiation, consistent with the result of visual inspection in Fig. 8(a), suggesting that the ZnO nanorods behaved as effective catalysts for photodegrading MO.

According to the Beer–Lambert law, the concentration of MO is linearly proportional to the intensity of the absorption peak at
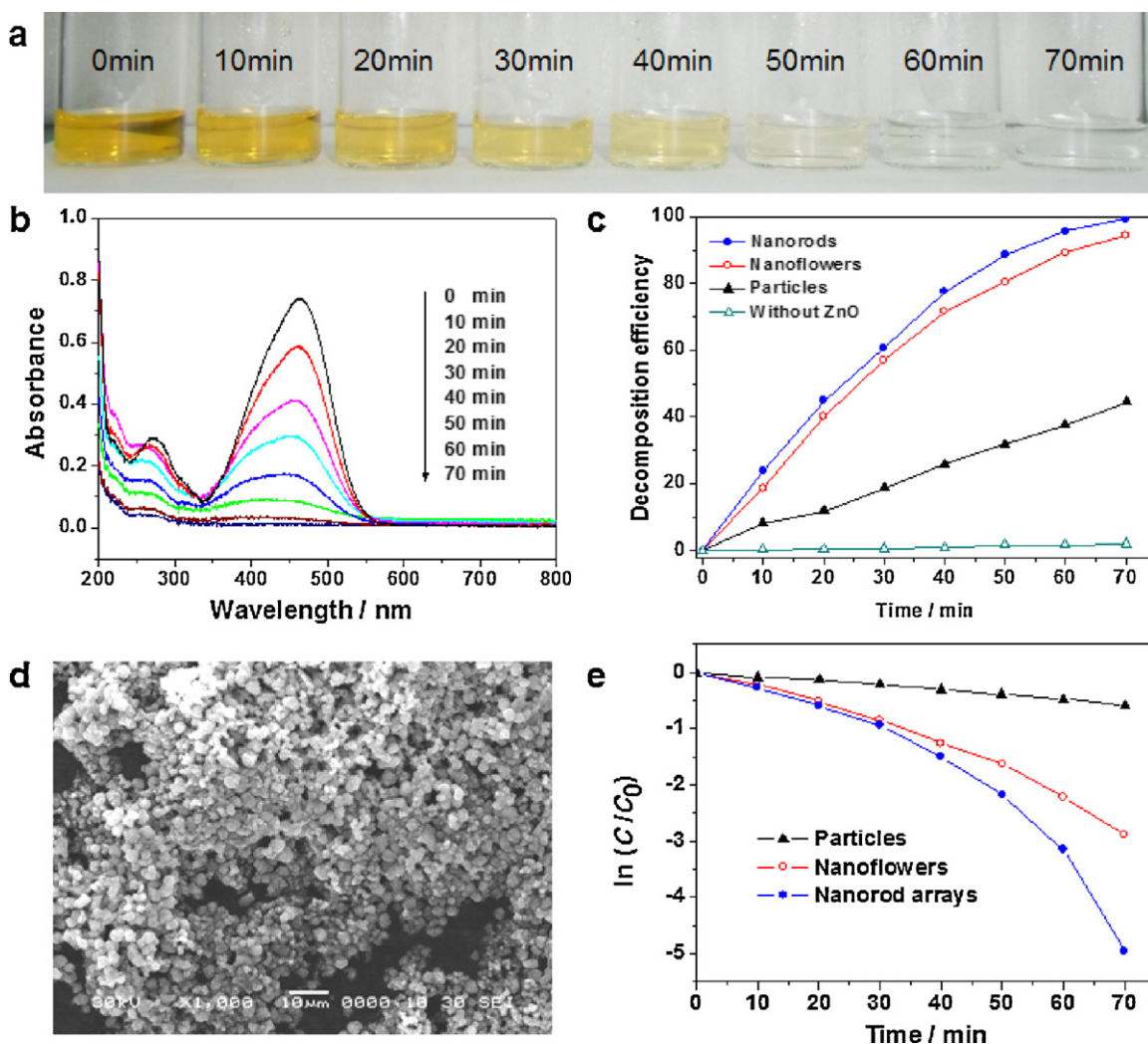
Fig. 8. (a) Photographs of methyl orange solutions upon photodegradation catalyzed by ZnO nanorod arrays, showing decolorization of the dye with time. (b) Spectral changes of MO solutions upon photodegradation catalyzed by ZnO nanorod arrays. (c) Comparison of decomposition efficiency of different ZnO samples for the degradation of methyl orange as well as that only induced by UV irradiation in the absence of any ZnO samples. (d) SEM image of the commercial ZnO particles. (e) Photodegradation kinetics of MO in the presence of ZnO micro/nanostructures.

462 nm, and thus the decomposition efficiency of MO can be calculated using the following expression:

$$\text{MO decomposition } (\%) = 100 \times \frac{C_0 - C}{C_0} \quad (1)$$

where C_0 and C are the equilibrium concentrations of MO before and after UV irradiation, respectively. Fig. 8(c) depicts the decomposition efficiency of MO over ZnO nanorods, nanoflowers, and commercial powders for comparison. Obviously, the ZnO nanorods exhibited the best photocatalytic activity, which was significantly higher than that of the ZnO nanochains [32] and comparable to that of Degussa P25 [33]. The photocatalytic performance of ZnO nanoflowers was still much superior to that of the commercial powders, which were composed of clumped particles with irregular shapes as shown in Fig. 8(d). This difference might be attributed to their larger specific surface area and one-dimensional characteristic of the nanorods and nanoflowers. However, the control experiment showed that MO molecules were very difficult to be decomposed only by UV irradiation without addition of ZnO samples, and the decomposition efficiency was merely 2% after UV irradiation for more than 1 h (Fig. 8c).

To quantitatively understand the reaction kinetics of MO degradation over different ZnO samples in our experiments, we re-plotted the data in Fig. 8(e) according to the pseudofirst-order kinetic model as expressed by Eq. (2), which is generally used for photocatalytic degradation process took place at the interface between the catalysts and the organic pollutants with low concentration [34].

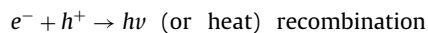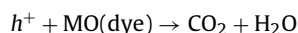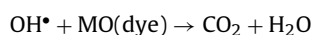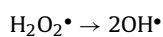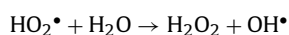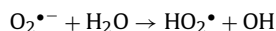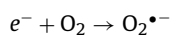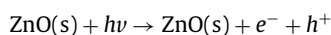$$\ln\left(\frac{C_0}{C}\right) = kt \quad (2)$$

where t is reaction time, k is the rate constant, C_0 and C are the concentrations of MO solution at time 0 and t, respectively. As can be seen, the photodecomposition reaction of MO molecules on the ZnO bulk powders followed the pseudofirst-order kinetics ($R^2 = 0.988$) with $k = 0.008$ min^{-1}, whereas those on the ZnO nanoflowers and nanorods deviated from the pseudofirst-order model. Probably this abnormal photocatalytic behavior of the prepared ZnO nanorods and hierarchical nanostructures was primarily caused by their morphologies and microstructures. More work is underway in our group to make it clear.

The photocatalytic decomposition process of MO molecules over ZnO nanostructures can be understood by the well-developed
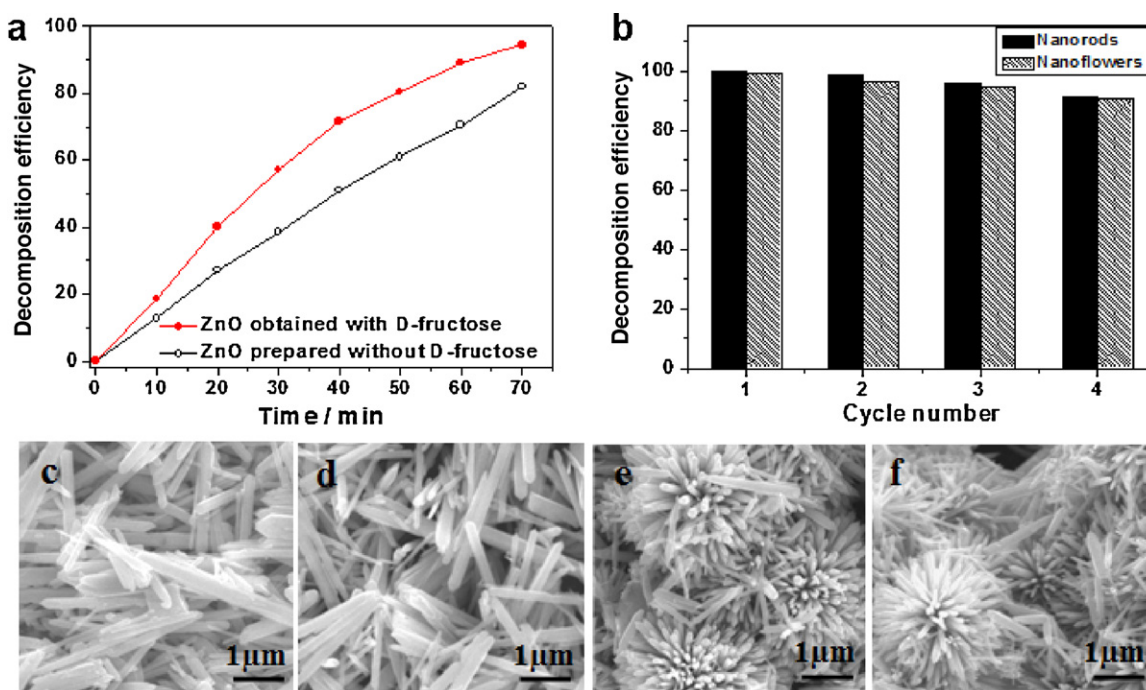
Fig. 9. (a) Comparison of the two kinds of ZnO nanoflowers prepared with or without D-fructose. (b) Cyclical stability of the ZnO photocatalysts. (c and d) SEM images of the ZnO nanorods before and after reused for 4 cycles, respectively. (e and f) SEM images of the ZnO nanoflowers before and after reused for 4 cycles, respectively.

mechanism of semiconductor photocatalysis as described as the following equations [35,36]. Upon UV light irradiation, electrons (e^-) in the valence band of ZnO were excited to the conduction band with the simultaneous generation of holes (h^+) in the valence band. The photogenerated electrons could be readily trapped by absorbed O_2 at the catalyst surface or the dissolved oxygen to yield superoxide radical anions ($O_2^{\bullet-}$). Subsequently, $O_2^{\bullet-}$ was transformed into hydroperoxy radical ($HO_2^\bullet$) and hydroxyl radical ($OH^\bullet$), which was a strong oxidizing agent to decompose the organic dye such as methyl orange (MO) [36]. Meanwhile, the photogenerated holes were trapped by surface hydroxyl groups (or H_2O) at the catalyst surface to yield hydroxyl radicals ($OH^\bullet$), or directly trapped by organic pollutions to further oxidize organic pollutants [35]. Of course, the electron–hole recombination was always unavoidable. On the basis of the proposed photocatalytic degradation mechanism, the higher the specific surface area was, the more oxygen molecules were absorbed on the catalyst surface, and the more $OH^\bullet$ was produced. On the other hand, the faster the photogenerated carriers were transported, the better the photocatalytic activity was. Therefore, the ZnO samples exhibited different photocatalytic activities in our experiments due to their different microstructures and specific surface areas.

$$ZnO(s) + h\nu \rightarrow ZnO(s) + e^- + h^+$$

$$e^- + O_2 \rightarrow O_2^{\bullet-}$$

$$O_2^{\bullet-} + H_2O \rightarrow HO_2^\bullet + OH$$

$$HO_2^\bullet + H_2O \rightarrow H_2O_2 + OH^\bullet$$

$$H_2O_2^\bullet \rightarrow 2OH^\bullet$$

$$h^+ + OH^- \rightarrow OH^\bullet$$

$$OH^\bullet + MO(dye) \rightarrow CO_2 + H_2O$$

$$h^+ + MO(dye) \rightarrow CO_2 + H_2O$$

$$e^- + h^+ \rightarrow h\nu \ (or \ heat) \ recombination$$

Considering that D-fructose was used to prepare the ZnO nanorod arrays and nanoflowers, we also investigated the possible effect of D-fructose on the photocatalytic activity of the ZnO catalysts. Because ZnO nanoflowers were always obtained whether D-fructose was added or not, and their morphology and microstructure did not change with the amount of D-fructose, we compared the photocatalytic activity of the two kinds of ZnO nanoflowers, which were prepared with or without addition of D-fructose, respectively. The result is shown in Fig. 9(a), suggesting that the accession of D-fructose for the synthesis of ZnO photocatalysts slightly enhanced the photocatalytic activity, owing to the doping of trace amount of carbon produced by pyrolysis of D-fructose as discussed in Section 3.2.

From a practical point of view, photo-dissolution of ZnO photocatalysts is an important concern due to the possible results of activity deterioration and secondary pollution from the dissolved Zn^{2+} [37]. Therefore, the cyclical stability of the ZnO catalysts was investigated and the results are shown in Fig. 9(b). In our experiments, the ZnO catalysts was separated via centrifugation each time, and reused for 4 cycles. From the quantitative measurements in Fig. 9(b) one can see that the decomposition efficiency of MO over the ZnO nanorods and nanoflowers after 4 cycles was 91.5% and 90.5%, respectively. The observed catalyst inactivation might be partially caused by photo-corrosion or photo-dissolution of the ZnO catalysts. SEM images of the ZnO nanorods before (Fig. 9c) and after 4 cycles (Fig. 9d) showed that the morphology of the nanorod-catalysts was almost unchanged during the process of recycling. However, disfigurement could be easily observed for the ZnO nanoflowers as shown in Fig. 9(e) and (f) after being recycled for 4 times, resulting in lower decomposition efficiency than that for the ZnO nanorods. This result indicated that photo-dissolution
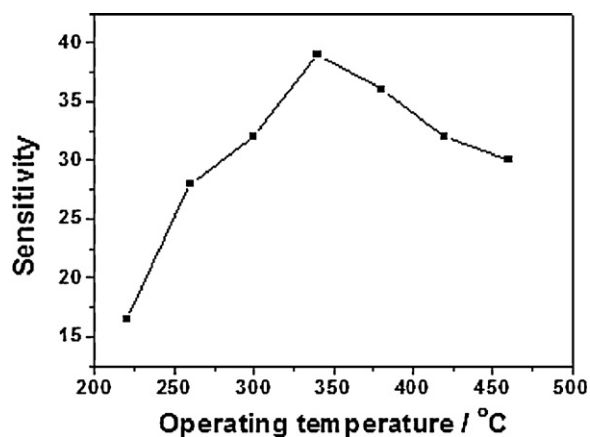
Fig. 10. Temperature-dependent sensing behavior of the ZnO nanorod arrays to 1000 ppm ethanol.

did occur for the as-prepared ZnO nanostructures, but it was much better than the reported ZnO film [37] and nanoparticles [38].

3.4. Gas sensing performance of the ZnO samples

Considering the sensitivity of a gas sensor is greatly influenced by operating temperature, we have first investigated the

temperature-dependent sensing behavior of the ZnO nanorod arrays to 1000 ppm of ethanol, and the results are depicted in Fig. 10. It can be seen that the sensitivity increased with the operating temperature and reached a maximum value of 39 at ~340 °C. Further measurements showed that both the nanorod arrays and the nanoflowers exhibited maximum sensitivity towards methanol, ethanol, isopropanol, acetone, and acetic acid in the temperature range of 320–360 °C. Thereafter, the best operating temperature was determined to be 340 °C for the sensing measurements of the ZnO nanostructures.

Fig. 11(a) depicts the real-time gas sensing performance of the ZnO nanorod arrays and nanoflowers upon cycling between increasing concentrations of ethanol and ambient air. As can be seen, both nanorod arrays and nanoflowers exhibited high sensitivity with the same value of about 3.96–5 ppm of ethanol vapor. The response and recovery time (defined as the time need to reach 90% of the final equilibrium value) are 5 s and 7 s, respectively, which are much less than those for the ZnO porous nanoplates-based sensors [39], indicating super-rapid response–recovery characteristics of the ZnO nanosensors. In addition, their sensitivities increased dramatically with the concentration of ethanol vapor. When the concentration of ethanol increased to 20 ppm, the sensitivity for the nanorod arrays and nanoflowers reached respectively to 8.7 and 10.9, comparable to that for the ZnO nanowires fabricated with microelectromechanical system [40]. However, the nanoflowers displayed larger amplitude of increase in sensitivity towards
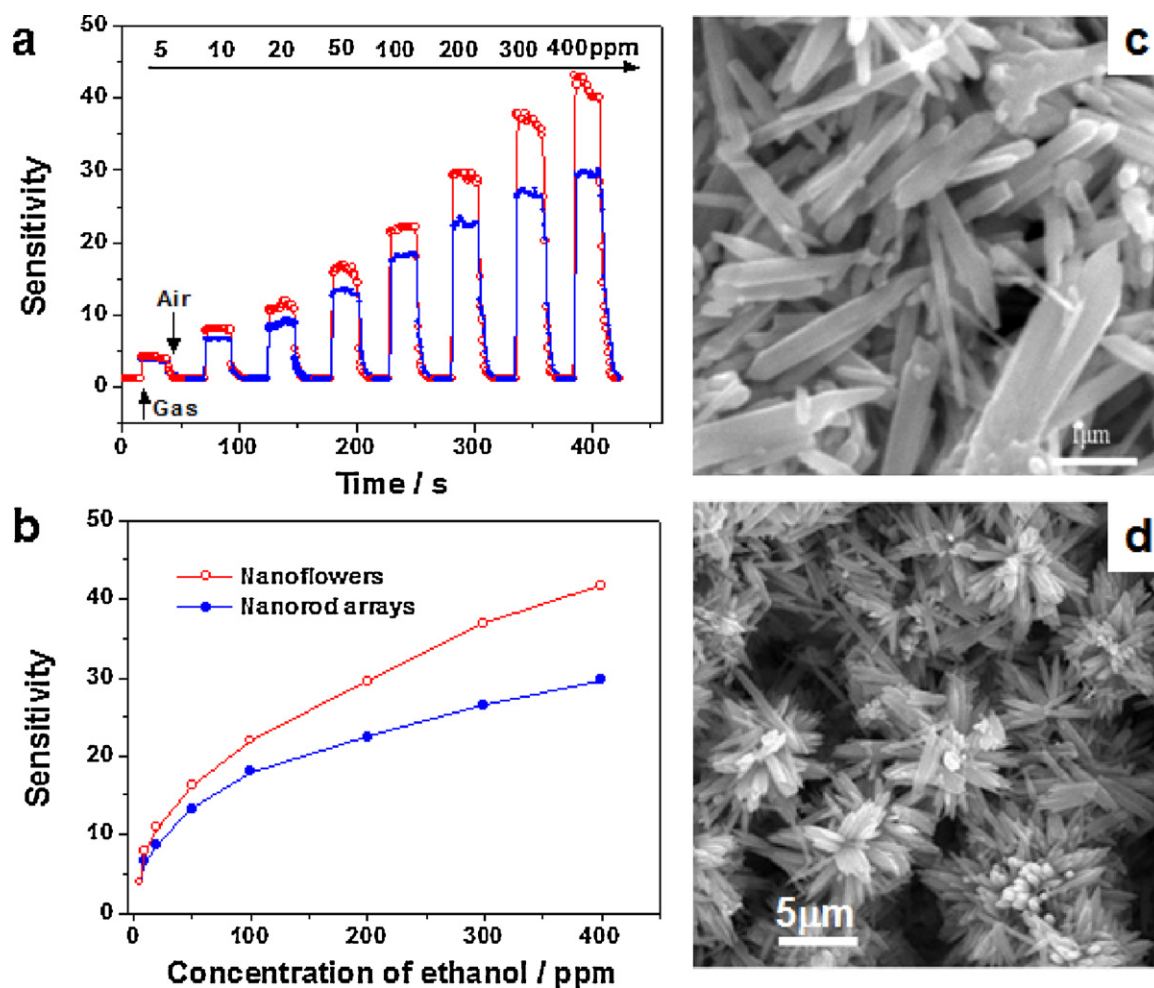

Fig. 11. (a) Temporal response of the sensors based on the ZnO nanorod arrays (solid circles) and nanoflowers (open circles) to ethanol gas in air. (b) Concentration-dependent sensing behavior of the ZnO-based sensors. SEM images of the films based on the nanorod arrays (d) and nanoflowers (e) coated on the sensor devices by ultrasonically dispersing the samples in distilled water.
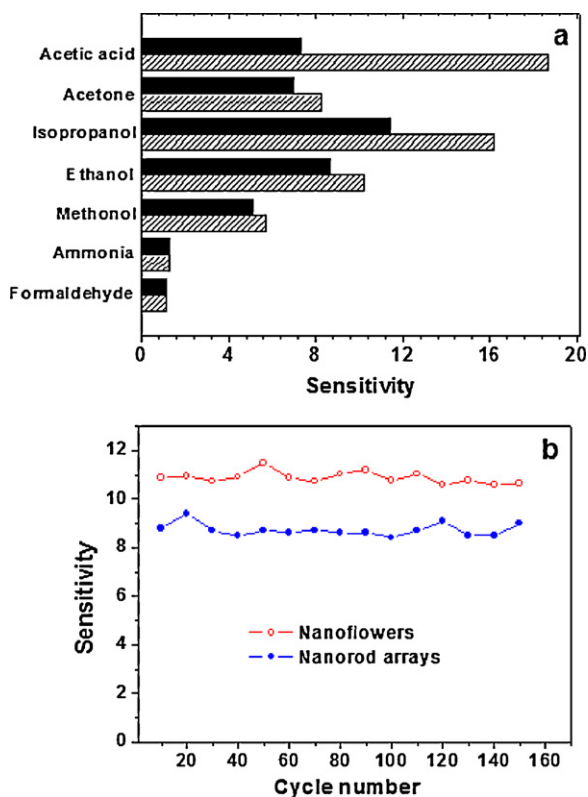
Fig. 12. (a) Selectivity of the ZnO-based sensors made of nanorod arrays (black) and nanoflowers (slash) towards different test gases in air with a concentration of 20 ppm. (b) Stability of the ZnO nanostructure-based sensors to 20 ppm of ethanol at 340 °C.

ethanol with higher concentration than the nanorod arrays did. This difference in sensing performance between nanoflowers and nanorod arrays is clearly shown in Fig. 11(b). To some extent, specific surface area of the solid powders (20.2 and 24.5 $m^2\,g^{-1}$ for the nanorods and nanoflowers, respectively) can be used as a reference to explain their performance difference. Another cause for concern might be the structural discrepancy in the films deposited on the sensors [41], as shown in Fig. 11(c) and (d). It can be seen that the nanorod arrays did not keep their ordered arrangement due to the ultrasonic treatment before coating, leading to the formation of relatively compact film and to loss of their intrinsic advantage for analyte transport [17]; while the nanoflowers still maintained their initial hierarchical morphology in the deposited film, resulting in high pore density, enlarged pore size, enhanced surface accessibility, and thus higher sensitivity [41].

As important parameters for practical applications, selectivity and long-term stability of the ZnO nanostructures-based sensors were also investigated and shown in Fig. 12. As can be seen from Fig. 12(a), both of the nanorod arrays and nanoflowers-based sensors were insensitive to formaldehyde and ammonia, while highly sensitive to alcohols such as methanol, ethanol and isopropanol with significantly increased sensitivity in this order. This phenomenon can be explained by the oxygen-vacancy model or reduction–reoxidation sensing mechanism [41]. Because ZnO is a typical *n*-type semiconductor, its conductivity is increased upon contact with reducing analytes such as alcohols. Methyl, ethyl and isopropyl in the tested alcohols acted as electron donating groups, and exhibited enhanced electron-denoting ability in sequence. Therefore, greatest change in conductivity and highest sensitivity were observed when the ZnO-based sensors contacted with isopropanol. In addition, both types of ZnO sensors exhibited impressive sensitivity to acetone, indicating their potential appli-

cations in modern breath analysis for disease diagnosis [41]. It is interesting that the ZnO nanoflowers-based sensor exhibited super high sensitivity to acetic acid, possibly due to the strong coordination ability of carboxylate anions. Similar results have been reported for other metal oxide nanostructures [42]. Note again that the sensing performance of the prepared ZnO nanoflowers were always superior to that of the ZnO nanorod arrays towards all the investigated gases. In addition, both the ZnO nanorod arrays and the nanoflowers-based sensors could be continuously operated over many cycles without loss of sensitivity as depicted in Fig. 12(b), and the results could be repeated after four months, illustrating good reproducibility and long-term stability of the nanosensors.

4. Conclusion

In summary, ZnO nanorod arrays and hierarchical nanostructures were successfully grown on various substrates including conductive/nonconductive and rigid/flexible ones through a simple one-step hydrothermal route without using any catalysts, surfactants and seed-coated layers. At the same time, ZnO nanoflowers composed of nanorods were obtained at the bottom of the autoclaves in the presence or absence of substrates. The crystallographic phase, morphology, and microstructure were characterized by XRD, EDS, SEM, TEM/HRTEM, and SAED. On the basis of the experimental data an in situ spontaneous-seeds-assisted growth mechanism was proposed for explaining the growth of ZnO nanostructures, and the role of D-fructose played was explored. In addition, both of the ZnO nanorod arrays and nanoflowers were investigated for potential applications in environmental remediation and monitoring. The results showed that the nanorod arrays exhibited better photocatalytic activity for photodegradation of methyl orange and impressive gas sensing performance towards alcohols, while the nanoflowers demonstrated enhanced gas sensing performance towards acetic acid. This suggested that the microstructure and morphology of the products had an important influence on their photocatalytic and sensing properties.

References

[1] Y.N. Xia, P.D. Yang, Y.G. Sun, Y.Y. Wu, B. Mayers, B. Gates, Y.D. Yin, F. Kim, H.Q. Yan, One-dimensional nanostructures: synthesis, characterization, and applications, Adv. Mater. 15 (2003) 353–389.
[2] C.N.R. Rao, F.L. Deepak, G. Gundiah, A. Govindaraj, Inorganic nanowires, Prog. Solid State Chem. 31 (2003) 5–147.
[3] Y. Li, F. Qian, J. Xiang, C.M. Lieber, Nanowire electronic and optoelectronic devices, Mater. Today 9 (2006) 18–27.
[4] Z.R.R. Tian, J.A. Voigt, J. Liu, B. Mckenzie, M.J. Mcdermott, M.A. Rodriguez, H. Konishi, H.F. Xu, Complex and oriented ZnO nanostructures, Nat. Mater. 2 (2003) 821–826.
[5] J.Y. Lao, J.G. Wen, Z.F. Ren, Hierarchical ZnO Nanostructures, Nano Lett. 2 (2002) 1287–1291.
[6] X.D. Wang, J.H. Song, J. Liu, Z.L. Wang, Direct-current nanogenerator driven by ultrasonic waves, Science 316 (2007) 102–105.
[7] X.S. Fang, L.M. Wu, L.F. Hu, ZnS nanostructure arrays: a developing material star, Adv. Mater. 23 (2011) 585–598.
[8] L. Vayssieres, M. Graetzel, Highly ordered SnO2 nanorod arrays from controlled aqueous growth, Angew. Chem. Int. Ed. 43 (2004) 3666–3670.
[9] H.D. Yu, Z.P. Zhang, M.Y. Han, X.T. Hao, F.R. Zhu, A general low-temperature route for large-scale fabrication of highly oriented ZnO nanorod/nanotube arrays, J. Am. Chem. Soc. 127 (2005) 2378–2379.
[10] W.X. Zhang, S.H. Yang, In situ fabrication of inorganic nanowire arrays grown from and aligned on metal substrates, Acc. Chem. Res. 42 (2009) 1617–1627.

[11] L. Li, T.Y. Zhai, H.B. Zeng, X.S. Fang, Y. Bando, D. Golberg, Polystyrene sphere-assisted one-dimensional nanostructure arrays: synthesis and applications, J. Mater. Chem. 21 (2011) 40–56.

[12] M.H. Huang, S. Mao, H. Feick, H.Q. Yan, Y.Y. Wu, H. Kind, E. Weber, R. Russo, P.D. Yang, Room-temperature ultraviolet nanowire nanolasers, Science 292 (2001) 1897–1899.

[13] J.X. Wang, X.W. Sun, Y. Yang, H. Huang, Y.C. Lee, O.K. Tan, L. Vayssieres, Hydrothermally grown oriented ZnO nanorod arrays for gas sensing applications, Nanotechnology 17 (2006) 4995–4998.

[14] K. Yang, G.W. She, H. Wang, X.M. Ou, X.H. Zhang, C.S. Lee, S.T. Lee, ZnO nanotube arrays as biosensors for glucose, J. Phys. Chem. C 113 (2009) 20169–20172.

[15] M.C. Mcalpine, H. Ahmad, D.W. Wang, J.R. Heath, Highly ordered nanowire arrays on plastic substrates for ultrasensitive flexible chemical sensors, Nat. Mater. 6 (2007) 379–384.

[16] Z.L. Wang, J.H. Song, Piezoelectric nanogenerators based on zinc oxide nanowire arrays, Science 312 (2006) 242–246.

[17] M. Law, L.E. Greene, J.C. Johnson, R. Saykally, P.D. Yang, Nanowire dye-sensitized solar cells, Nat. Mater. 4 (2005) 455–459.

[18] C.J. Lee, T.J. Lee, S.C. Lyu, Y. Zhang, H. Ruh, H.J. Lee, Field emission from well-aligned zinc oxide nanowires grow at low temperature, Appl. Phys. Lett. 81 (2001) 3648–3650.

[19] D.K. Hwang, S.H. Kang, J.H. Lim, E.J. Yang, J.Y. Oh, J.H. Yang, S.J. Park, p-ZnO/n-GaN heterostructure ZnO light-emitting diodes, Appl. Phys. Lett. 86 (2005) 222101–222103.

[20] O. Akhavan, M. Mehrabian, K. Mirabbaszadeh, R. Azimirad, Hydrothermal synthesis of ZnO nanorod arrays for photocatalytic inactivation of bacteria, J. Phys. D: Appl. Phys. 42 (2009) 225305–225314.

[21] D.I. Suh, S.Y. Lee, J.H. Hyung, T.H. Kim, S.K. Lee, Multiple ZnO nanowires field-effect transistors, J. Phys. Chem. C 112 (2008) 1276–1281.

[22] Z. Jehl, J. Rousset, F. Donsanti, G. Renou, N. Naghavi, D. Lincot, Electrodeposition of ZnO nanorod arrays on ZnO substrate with tunable orientation and optical properties, Nanotechnology 21 (2010) 395603–395608.

[23] X.L. Wang, H. Zhu, W. Yang, F. Yang, X.R. Yang, Rapid and tunable patterning of high purity ZnO nanoarrays without template or catalyst, Chem. Eur. J. 15 (2009) 4253–4257.

[24] H.Q. Le, S.J. Chua, K.P. Loh, E.A. Fitzgerald, Y.W. Koh, Synthesis and optical properties of well aligned ZnO nanorods on GaN by hydrothermal synthesis, Nanotechnology 17 (2006) 483–488.

[25] C.L. Ren, B.F. Yang, M. Wu, J. Xu, Z.P. Fu, Y. Lv, T. Guo, Y.X. Zhao, C.Q. Zhu, Synthesis of Ag/ZnO nanorods array with enhanced photocatalytic performance, J. Hazard. Mater. 182 (2010) 123–129.

[26] T. Pauporte, G. Bataille, L. Joulaud, F.J. Vermersch, Well-aligned ZnO nanowire arrays prepared by seed-layer-free electrodeposition and their Cassie–Wenzel transition after hydrophobization, J. Phys. Chem. C 114 (2010) 194–202.

[27] F. Xu, Y. Lu, Y. Xie, Y. Liu, Seed layer-free electrodeposition and characterization of vertically aligned ZnO nanorod array film, J. Solid State Electrochem. 14 (2010) 63–70.

[28] Q. Ahsanulhaq, J.H. Kim, J.H. Kim, Y.B. Hahn, Seedless pattern growth of quasi-aligned ZnO nanorod arrays on cover glass substrates in solution, Nanoscale Res. Lett. 5 (2010) 669–674.

[29] X.L. Gou, R. Li, G.X. Wang, Z.X. Chen, D. Wexler, Room-temperature solution synthesis of Bi$_2$O$_3$ nanowires for gas sensing application, Nanotechnology 20 (2009) 495501–495505.

[30] C.H. Fang, B.Y. Geng, J. Liu, F.M. Zhan, D-Fructose molecule template route to ultra-thin ZnSnO$_3$ nanowire architectures and their application as efficient photocatalyst, Chem. Commun. 17 (2009) 2350–2352.

[31] C.H. Yao, Y. Shin, L.Q. Wang, C.F. Windisch, W.D. Samuels, B.W. Arey, C.M. Wang, W.M. Risen, G.J. Exarchos, Hydrothermal dehydration of aqueous fructose solutions in a closed system, J. Phys. Chem. C 111 (2007) 15141–15145.

[32] M. Dutta, D. Basak, A novel and simple method to grow beaded nanochains of ZnO with superior photocatalytic activity, Nanotechnology 20 (2009) 475602–475608.

[33] Z.K. Zheng, B.B. Huang, X.Y. Qin, X.Y. Zhang, Y. Dai, Strategic synthesis of hierarchical TiO$_2$ microspheres with enhanced photocatalytic activity, Chem. Eur. J. 16 (2010) 11266–11270.

[34] C.H. An, S. Peng, Y.G. Sun, Facile synthesis of sunlight-driven AgCl:Ag plasmonic nanophotocatalyst, Adv. Mater. 22 (2010) 2570–2574.

[35] Y. Zheng, C. Chen, Y. Zhan, X. Lin, Q. Zheng, K. Wei, J. Zhu, Y.J. Zhu, Luminescence and photocatalytic activity of ZnO nanocrystals: correlation between structure and property, Inorg. Chem. 46 (2007) 6675–6682.

[36] J. Mu, C. Shao, Z. Guo, Z. Zhang, M. Zhang, P. Zhang, B. Chen, Y. Liu, High photocatalytic activity of ZnO-carbon nanofiber heteroarchitectures, ACS Appl. Mater. Interfaces 3 (2011) 590–596.

[37] J. Han, W. Qiu, W. Gao, Potential dissolution and photo-dissolution of ZnO thin films, J. Hazard. Mater. 178 (2010) 115–122.

[38] H. Fu, T. Xu, S. Zhu, Y.F. Zhu, Photocorrosion inhibition and enhancement of photocatalytic activity for ZnO via hybridization with C60, Environ. Sci. Technol. 42 (2008) 8064–8069.

[39] Z.H. Jing, J.H. Zhan, Fabrication and gas-sensing properties of porous ZnO nanoplates, Adv. Mater. 20 (2008) 4547–4551.

[40] Q. Wan, Q.H. Li, Y.J. Chen, T.H. Wang, Fabrication and ethanol sensing characteristics of ZnO nanowire gas sensors, Appl. Phys. Lett. 84 (2004) 3654–3656.

[41] A. Tricoli, M. Righettoni, A. Teleki, Semiconductor gas sensors: dry synthesis and application, Angew. Chem. Int. Ed. 49 (2010) 7632–7659.

[42] X.L. Gou, G.X. Wang, J. Park, H. Liu, J. Yang, Monodisperse hematite porous nanospheres: synthesis, characterization, and applications for gas sensors, Nanotechnology 19 (2008) 125606–125612.